Direct mass measurement of ^{91}Rh and ^{89}Ru and mid-shell trend of the one-proton separation energies for $N = Z + 1$ nuclei

Samuel Ayet San Andrés,[1,*] Meetika Narang,[2,3] Gabriella Kripkó-Koncz,[4,5,6] Zhuang Ge,[2,7,8] Nived Keeppalli,[4,2,5] Daler Amanbayev,[4,2,5] Wolfgang R. Plaß,[2,4] Timo Dickel,[2,4] Emma Haettner,[2] Christine Hornung,[4,2] Nicolas Hubbard,[2] Anu Kankainen,[7,8] Debodyuti Kar,[9,2] Kriti Mahajan,[4,5] Israel Mardor,[10,11] Ali Mollaebrahimi,[4] David J. Morrissey,[12] Christoph Scheidenberger,[2,4,5] Makar Simonov,[4,5] Nazarena Tortorelli,[13,2] Jianwei Zhao,[2,14] Jasmiina Ahokas,[7,8] Alejandro Algora,[1,15] Faraz Amjad,[2] Juha Äystö,[7,8] Soumya Bagchi,[9] Martin Bajzek,[2] Sönke Beck,[2,4] Olga Beliuskina,[7,8] Julian Bergmann,[4] Andrey Blazhev,[16] Jeroen Peter Bormans,[2,17,5] Ziga Brencic,[18,19] Volha Charviakova,[20] Paul Constantin,[21] Justus Eder,[2] Tommi Eronen,[7,8] Martina Feijoo-Fontán,[22] Hans Geissel,[2,4,†] Simeon Glöckner,[2] Pablo Gonzalez Rusell,[23,22] Magdalena Górska,[2] Antia Graña-González,[23] Florian Greiner,[4] Lizzy Gröf,[4] Jan Hetzel,[2] Nasser Kalantar-Nayestanaki,[3] Annesha Karmakar,[2] Luke Kilmartin,[24,2] Ronja Knöbel,[2] Daria Kostyleva,[2,4] Natalia Kuzminchuk,[2] Ivan Mukha,[2] Tobias Murböck,[4] Dimitrii Nesterenko,[7] David Ondreka,[2] Zygmunt Patyk,[20] Aaron Pieper,[4] Stephane Pietri,[2] Ilkka Pohjalainen,[7] Rinku Prajapat,[2,25] Martha Reece,[2] Moritz Pascal Reiter,[6] Mikael Reponen,[7,8] Elena Rocco,[2] Jose Luis Rodríguez-Sánchez,[23,22] Pratap Roy,[26] Suraj Kumar Singh,[2,4] Peter Spiller,[2] Jens Stadlmann,[2] Alexandru State,[21] Ionut C. Stefanescu,[27,‡] Yoshiki K. Tanaka,[2,28] Matjaž Vencelj,[18] Ville Virtanen,[7,8] Helmut Weick,[2] Leonard Welde,[4] Heinrich Wilsenach,[11] Kathrin Wimmer,[2] Jan Wirtz,[2,17] and Jiajun Yu[2,29,†]

(for the Super-FRS Experiment Collaboration)

[1]*Instituto de Física Corpuscular, CSIC - Universidad de Valencia, 46980 Valencia, Spain*

[2]*GSI Helmholtzzentrum für Schwerionenforschung GmbH, 64291 Darmstadt, Germany*

[3]*ESRIG, University of Groningen, 9747 AA Groningen, The Netherlands*

[4]*II. Physikalisches Institut, Justus-Liebig-Universität Gießen, 35392 Gießen, Germany*

[5]*Helmholtz Research Academy Hesse for FAIR (HFHF), GSI Helmholtz Center for Heavy Ion Research, Campus Gießen, D-35392 Gießen, Germany*

[6]*School of Physics and Astronomy, University of Edinburgh, EH9 3FD Edinburgh, United Kingdom*

[7]*University of Jyväskylä, 40014 Jyväskylä, Finland*

[8]*Helsinki Institute of Physics, 00014 Helsinki, Finland*

[9]*Department of Physics, IIT-ISM Dhanbad, Jharkhand 826004, India*

[10]*Soreq Nuclear Research Center, 81800 Yavne, Israel*

[11]*Racah Institute of Physics, The Hebrew University of Jerusalem, Jerusalem 9190401, Israel*

[12]*Michigan State University, 48824 East Lansing, Michigan, USA*

[13]*Ludwig Maximilian University of Munich, 80539 München, Germany*

[14]*School of Physics, Beihang University, Beijing 100191, China*

[15]*HUN-REN Institute for Nuclear Research (ATOMKI), H-4001 Debrecen, Hungary*

[16]*Institute for Nuclear Physics, University of Cologne, 50937 Cologne, Germany*

[17]*Institut für Kernphysik, Technische Universität Darmstadt, 64289 Darmstadt, Germany*

[18]*Jozef Stefan Institute, SI-1000 Ljubljana, Slovenia*

[19]*Faculty of Mathematics and Physics, University of Ljubljana, 1000 Ljubljana, Slovenia*

[20]*National Centre for Nuclear Research, Hoża 69, 00-681 Warszawa, Poland*

[21]*Extreme Light Infrastructure - Nuclear Physics, IFIN-HH, 30 Reactorului Street, 077125, Magurele, Romania*

[22]*IGFAE, Universidade de Santiago de Compostela, E-15782 Santiago de Compostela, Spain*

[23]*CITENI, Campus Industrial de Ferrol, Universidade da Coruña, E-15403 Ferrol, Spain*

[24]*School of Physics, University College Dublin, D04 N2E5 Dublin, Ireland*

[25]*Astronomy and Physics Department, Saint Mary's University, Halifax, Nova Scotia B3H 3C3, Canada*

[26]*Variable Energy Cyclotron Centre, 1/AF–Bidhan Nagar, 700064 Kolkata, India*

*Contact author: samuel.ayet@uv.es

†Deceased.

‡Present address: Institut für Kernphysik, Technische Universität Darmstadt, 64289 Darmstadt, Germany.

[27]*Horia Hulubei National Institute of Physics and Nuclear Engineering (IFIN-HH), 077125 Măgurele, Romania*
[28]*High Energy Nuclear Physics Laboratory, RIKEN, 2-1 Hirosawa, Wako, 351-0198 Saitama, Japan*
[29]*Institute of Modern Physics - Chinese Academy of Science, 730000 Lanzhou, China*

(Received 23 April 2026; accepted 31 July 2026; published 8 September 2026)

Neutron-deficient nuclei in the $N \approx Z$, $A \approx 90$ region were produced by fragmentation of a relativistic ^{107}Ag beam at the GSI Helmholtz Centre for Heavy Ion Research (GSI), separated in the fragment separator FRS, slowed down, and thermalized, and high-precision mass measurements were performed employing the multiple-reflection time-of-flight mass spectrometer (MR-TOF-MS) of the FRS Ion Catcher. The masses of ^{91,93,95}Rh, ^{89}Ru, ^{88}Tc, ^{87,88,89}Mo, and ^{87,88,89}Nb were determined. The mass of ^{91}Rh was measured for the first time. For ^{89}Ru, the measured mass excess deviates by more than ten standard deviations (361 keV) from the previous measurement. A possible misidentification of the measured nuclei, including ^{89}Ru, with contaminants was excluded using a newly developed identification technique for MR-TOF-MS measurements. For the other nuclides, the measured masses agree well with previous measurements. The impact of the new masses on the one-proton separation energy (S_p) of the nuclei with constant total isospin projection (T_z) in the island of inversion around $N = Z = 40$ is investigated, and signatures of the deformed shell gap at $Z = 38$ are found. A comparison of the experimental S_p values with the predictions of several mass models shows a general agreement of the trends.

DOI: 10.1103/lsp5-qntn

I. INTRODUCTION

Exotic nuclei far from the valley of β stability are known to exhibit striking phenomena, including the unusual evolution of nuclear shell closures [1,2]. These effects are often associated with the appearance of deformed nuclear shapes even at low excitation energies near closed shells. The corresponding regions of the nuclear chart are known as "islands of inversion" [3,4]. The island of inversion around $N = Z = 40$ is particularly rich in nuclear structure effects; nuclei in this region of the nuclear chart exhibit rapid shape changes, and states corresponding to spherical and deformed shapes are expected to coexist at low energies [4–10]. While the nuclei near $N = Z = 34$–35 are often associated with oblate deformations [9,10], in the nuclei around $N = Z = 38$–42 strongly deformed prolate shapes often coexist with nearly spherical shapes [4,8]. This large deformation is predicted to then decrease gradually towards the spherical, doubly magic ^{100}Sn [11,12]. In addition to the oblate-prolate shape transition at $N = Z = 36$, there have been experimental indications of significantly different nuclear shapes in the odd-odd $N = Z$ nuclides ^{70}Br ($Z = 35$) and ^{78}Y ($Z = 39$) and their neighboring even-even $N \approx Z$ nuclides, which, so far, could not be reproduced in theoretical calculations [8,11,13–16]. In addition to their nuclear shape, the empirical proton-neutron interaction strength [17] also shows different trends in odd-odd and even-even nuclei in the range $N = Z = 29$–37 [18,19]. This raises the question whether an odd-odd vs even-even staggering of nuclear observables occurs in this region of the nuclear chart.

Due to the wide variety and rapid changes of the observed nuclear structures and shapes in the island of inversion around $N = Z = 40$, measurements performed in this region of the nuclear chart provide important testing grounds for nuclear models [4,11,16,20–26]. These phenomena have been associated with the population of $1g_{9/2}$ intruder orbitals, the separation of which from the orbitals in the upper pf shell depends on the strength of the spherical $N = Z = 40$ shell gap [6,9,20]. In nuclei with similar numbers of protons and neutrons with isospin projection $T_z = (N - Z)/2$ close to zero, these phenomena are stronger due to similarities in the proton and neutron single-particle energies and, thus, the related shell effects reinforce one another [6,9,27].

The binding energy of the nucleons inside an atomic nucleus is directly related to its mass. It reflects the stability and structure of the nucleus and is a sensitive indicator of underlying shell effects and nuclear shape transitions [28]. Local trends of the binding-energy surface and its derivatives, e.g., the trends of nucleon separation energies for nuclides with constant isospin projection, can reveal information on the evolution of nuclear shell closures in exotic nuclei [29]. To this end, in this work, high-precision direct mass measurements of eleven neutron-deficient nuclides in the range $Z = 41$–45 are reported. The measured masses are then used to study the evolution of the one-proton separation energies (S_p) in nuclei with isospin projection $T_z = 1/2$ and to gain further insights on the island of inversion around $N = Z = 40$.

II. EXPERIMENTAL METHODS

A. The FRS and the FRS Ion Catcher

The mass measurements presented in this work were conducted using the FRS Ion Catcher [30,31] at the final focal plane of the fragment separator FRS [32] at the GSI Helmholtz Centre for Heavy Ion Research, Darmstadt, Germany, during two experimental campaigns (Experiment I and Experiment II). Exotic nuclei were produced by projectile fragmentation of a primary beam of ^{107}Ag at energies of 730 and 440 MeV/nucleon with intensities of approximately 1.5×10^9 and 1.8×10^{10} ions per spill on beryllium targets of 8045 and 1622 mg/cm^2 thickness in Experiments I and II, respectively. The boost in the intensity of the primary beam in Experiment II was achieved by not stripping the ions prior to injection into the heavy ion synchrotron SIS18. This is one of the measures that will be employed to enable high primary beam intensities for the upcoming FAIR facility. At the moment, this means a reduction of the primary beam energy; however, at FAIR, a higher beam energy along with enhanced intensity will be available due to the new SIS100 synchrotron [33]. Lower beam energies necessitate the use of thinner targets, which partially offsets the advantage of having a higher primary beam intensity; overall, for Experiment II, an increase in the production yield by a factor of 2 to 5 (depending on the nuclei) could be expected compared to Experiment I, taking into account both a thinner target and an enhanced beam intensity. The cocktail of fragments was separated in flight in the FRS, which was operated in monochromatic mode with an aluminum degrader (735 mg/cm^2) at the central focal plane. In Experiment I, the high-transmission mode [34] of the FRS was used, while in Experiment II the standard mode was employed. The target thickness was chosen such that the isotones have the same stopping range for a given primary beam energy, similar to [35].

The projectile fragments were delivered to the FRS Ion Catcher, slowed down in a homogeneous degrader and thermalized in the cryogenic stopping cell (CSC) [36–38]. The CSC was filled with ultrapure helium at a pressure of 52 and 89 mbar and a temperature of 89 and 86 K, corresponding to an areal density of 2.8 and 5.0 mg/cm^2 in the Experiments I and II, respectively. Finally, the ions were transferred through the radio-frequency quadrupole (RFQ) beamline to the multiple-reflection time-of-flight mass-spectrometer (MR-TOF-MS) [39–41], where high-resolution mass measurements were conducted. The total efficiency of the FRS Ion Catcher was not determined in these experiments, but it typically amounts to about 0.2% [42]. In both experiments, the MR-TOF-MS was operated with a repetition rate of 50 Hz. The ions in the mass range of interest performed about 265 to 275 turns in the analyzer of the MR-TOF-MS in Experiment I and about 470 to 490 turns in Experiment II. All ions measured in this work were singly positively charged. The mass-range selector (MRS) [41] in the MR-TOF-MS was used in both experiments to limit the mass-to-charge range of the measured ions. For the measurement of rhodium isotopes, a new operation mode of the MRS was implemented to select two narrow, separate mass-to-charge windows [42]. This operation mode allows to simultaneously measure calibrant ions with significantly different mass-to-charge ratios as compared to the ions of interest, or to measure the ion of interest with an adduct, without unnecessary background and ambiguities in the mass spectrum [43]. For the rhodium isotopes, the MRS was set to transport simultaneously $85 \leqslant A \leqslant 87$ and $90 \leqslant A \leqslant 91$ for ^{91}Rh, $84 \leqslant A \leqslant 87$ and $92 \leqslant A \leqslant 94$ for ^{93}Rh, and $84 \leqslant A \leqslant 87$ and $93 \leqslant A \leqslant 95$ for ^{95}Rh.

B. Data analysis procedure

The data analysis was performed using a well-established method described in Ref. [44]. A time-resolved calibration (TRC) was performed using ^{86}Kr and ^{85}Rb as calibrant ions for Experiments I and II, respectively, correcting for time-of-flight (TOF) drifts on the 10-second scale. For the multi-turn calibration (see Sec. IV of Ref. [44]) reference ions that cover a large number of different turn numbers were used; for Experiment I ^{85}Rb, ^{84}Kr ^{1}H, ^{87}Rb, ^{86}Kr ^{1}H and ^{88}Sr were used; for Experiment II ^{86}Kr and ^{87}Rb were used to obtain the mass of ^{89}Ru and ^{88}Tc, and ^{85}Rb, ^{86}Kr, ^{87}Rb and ^{90}Ru were used to obtain the mass of ^{91}Rh. The reference ions used in the final step of the analysis procedure, i.e., the precision calibration, are listed in Table I. The masses of all reference ions were taken from the Atomic Mass Evaluation AME2020 [45]. A hyperexponentially modified Gaussian (Hyper-EMG) [46] peak shape with two exponentials on the left and one exponential on the right side was employed for fitting the data obtained in both experiments, with parameters determined from peaks with a large number of events, i.e., ^{84}Kr ^{1}H for Experiment I and ^{87}Rb for Experiment II. The uncertainties of the measured mass values are mainly dominated by contributions related to the available statistics of the ions of interest, conversion of the time-of-flight spectrum into mass-to-charge ratio when calibrant and ion of interest perform different number of turns, and possible contaminants beneath the fitted peaks, including unresolved isomeric states, where applicable. Other systematic uncertainty contributions, including the ones related to the peak-shape determination and to switching the electrostatic mirrors of the time-of-flight analyzer, were found to be negligible in the experiments reported here. For the nuclides, which were measured in multiple experimental runs, the final mass values and uncertainties were determined based on averaging with the weighted mean and grouping the mass uncertainties deduced for the individual measurements into dependent and independent contributions [44].

The analysis of MR-TOF spectra is complicated by the fact that the mass lines of the ions do not necessarily need to appear in the TOF spectrum in the sequence of their mass-to-charge ratios. Lighter and thus faster ions can outstrip heavier and thus slower ions, such that they undergo different numbers of turns in the analyzer. Thus, the mass determination can only be achieved if for all relevant mass lines the respective numbers of turns have been determined. Misidentification of a mass line can occur if an unexpected contaminant ion species, which undergoes a different number of turns than an ion of interest (IOI), appears in the TOF spectrum at approximately the same TOF as the IOI, such that the mass line is erroneously assigned to the IOI instead of to the contaminant ion species.

This problem can be overcome by using the MRS to remove all ions that would undergo a different number of turns than the IOI. However, for high-resolution mass measurements, which necessitate a large number of turns, this leads to very small mass-to-charge windows, which may contain only one IOI and even lack a proper calibrant ion species. For broadband measurements, which have the important advantage that several of the IOIs produced can be measured simultaneously, the problem is usually solved in a different way [47]. Here, two measurements with different flight times are made, such that the IOIs differ in the number of turns between the two measurements. The correct assignment of the number of turns is then ensured by requiring that, for each identified ion species, a mass line is observed at the correct

TABLE I. Results obtained in this work together with the values given in the AME2020 [45] (# refers to an extrapolated value) for comparison. For every measured nuclide, the table shows the corresponding experiment, the reference ion used to perform the precision calibration, the number of turns the ion of interest underwent in the analyzer of the MR-TOF-MS, the number of events detected, the mass excess obtained in this work, the mass excess as published in the AME2020, and the difference between mass excess values obtained in this work and the ones published in the AME2020. For ^{89}Ru we provide all individual measurements as well as their average. See text for detailed information.

Nuclide	Experiment	Reference	Number of turns	Number of events	Mass excess FRS-IC (keV)	Mass excess AME2020 (keV)	Mass excess FRS-IC–AME2020 (keV)
^{95}Rh	II	^{87}Rb	486	264	−78 311(31)	−78 341(4)	31(32)
^{93}Rh	II	^{87}Rb	472	57	−68 993(30)	−69 011.8(26)	19(30)
^{91}Rh	II	^{87}Rb	477 & 482	44	−58 466(20)	−58 570(300)#	104(301)#
^{89}Ru	I	^{89}Y	275	24	−57 991(46)	−58 369(24)	378(52)
	I	^{89}Y	265	37	−57 992(42)		377(48)
	II	^{87}Rb	466	10	−58 036(40)		333(47)
	Average			71	−58 008(25)		361(35)
^{88}Tc[a]	I	^{84}Kr^{1}H	276 & 267			−61 670(4)	
	II	^{87}Rb	468				
	Average			532	−61 708(28)		−38(28)
^{89}Mo[b]	I	^{84}Kr^{1}H	265	10	−74 968(79)	−75 015(4)	47(79)
^{88}Mo	I	^{84}Kr^{1}H	276 & 267	50	−72 740(35)	−72 687(4)	−53(35)
^{87}Mo	I	^{84}Kr^{1}H	278 & 268	316	−66 866(19)	−66 884.8(29)	19(19)
^{89}Nb[a]	I	^{84}Kr^{1}H	275 & 265	18	−80 607(57)	−80 626(24)	19(62)
^{88}Nb[a]	I	^{84}Kr^{1}H	276 & 267	43	−76 160(80)	−76 170(60)	10(100)
^{87}Nb	I	^{84}Kr^{1}H	278 & 268	72	−73 905(25)	−73 874(7)	−31(26)

[a]The measurements of this nucleus have included additional uncertainty due to an unresolved isomer; see text for further details.
[b]One measurement from Experiment I had an overlap with the molecule $^{12}C_6{}^{13}C_1{}^{2}H_1$ ($A = 85$) performing a different turn number, therefore, it is discarded and only one measurement is reported.

position in both analyzed TOF mass spectra. If an IOI is identified in only one of the two spectra, its identification is rejected.

This approach, however, cannot exclude misidentification in all cases. (i) It might be that there are two unexpected contaminant ion species present in the two measurements, for which an assignment of turn numbers can be found such that an expected IOI is erroneously identified in both spectra. This is illustrated in Fig. 1. Panel (a) shows the mass distribution of the ions in the MR-TOF-MS, containing the position of the IOI where it would be observed if transmitted to the MR-TOF-MS, and two unexpected contaminant ion species U1 und U2. Two different TOF spectra are acquired with the IOI undergoing N turns in the first measurement and $N + n$ turns in the second measurement, with typically $n = 1$–5% of N. The panels (b) and (c) show the apparent mass spectra as obtained from the respective TOF spectra for N and $N + n$ turns, respectively. For the ion species U1, which undergoes an unknown number of turns, a turn number is assigned such that it appears at the mass-to-charge ratio of the IOI in (b), and for the ion species U2, which also undergoes an unknown number of turns, also a turn number is assigned such that it appears at the mass-to-charge ratio of the IOI in (c). In this case, the standard verification method cannot detect whether events for the IOI are present in the TOF spectra or not, unless the abundance ratio between the ion species provides an additional identification criterion. (ii) Furthermore, it may be that an IOI is correctly identified in both acquired spectra, but that its mass line overlaps too closely with an unexpected contaminant ion species to detect this overlap, leading to a shift in the determined mass value.

To reliably detect these cases, a new identification strategy called MAVERIC (Multiturn Analysis for VERification of identifIcation and exclusion of misidentifiCation) has been developed. To apply this method, two TOF spectra are acquired and the identification for each IOI is verified by ensuring its presence in both spectra, as in the standard approach. With the MAVERIC method, this verification is extended. For every mass line in the first TOF spectrum, the position in the second mass spectrum is checked for all possible turn numbers within the mass-to-charge range transmitted by the MRS, and vice versa. If this check shows that there is a second possibility for the identification of a mass line, this identification is rejected. In the example shown in Fig. 1, the misidentification of the IOI by the unexpected species U1 and U2 is detected and the measurement of the IOI is rejected. In this way, MAVERIC not only verifies that there is a mass line in both mass spectra that can be assigned to the IOI, but also excludes cases where the mass line assigned to the IOI can be due to an unexpected ion species. It also detects cases where the mass line assigned to the IOI may overlap with another ion species. Thus, it provides a significantly more reliable identification than the standard identification method, in particular in densely populated broadband mass spectra.

All the nuclides in this work with $87 \leqslant A \leqslant 91$ were measured with two different turn numbers, and the MAVERIC method was applied. The nuclides ^{89}Ru and ^{88}Tc were measured with an additional third turn number in Experiment II.

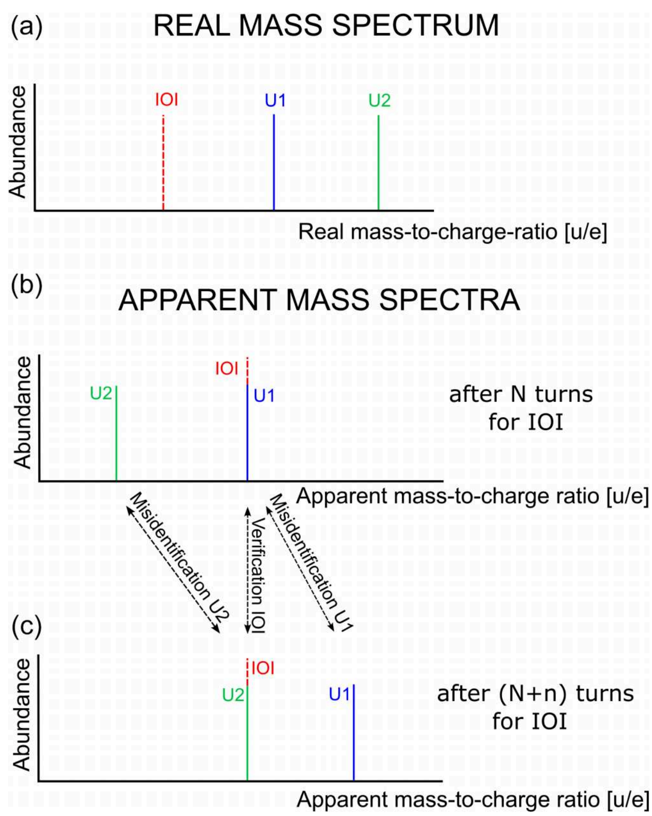

FIG. 1. The MAVERIC method explained graphically. Panel (a): Real mass spectrum showing the order of three ion species, the ion of interest (IOI), for which it is not known if it is present in the measurement or not, an unexpected ion species U1, and another unexpected ion species U2. Panels (b) and (c): Apparent mass spectra for N and $N + n$ turns, respectively. Note that the MAVERIC method is not limited to three different ion species, and that the order of ion species can be arbitrary. See text for further details.

Note that only one measurement is reported for ^{89}Mo because the second measurement has a strong overlap at a distance of about 100 keV, corresponding to about a third of the full width at half maximum (FWHM), with a more abundant $A = 85$ molecule ($^{12}C_6\,^{13}C_1\,^{2}H_1$) performing a different number of turns.

III. RESULTS

In this work, the masses of eleven nuclides were measured: ^{91,93,95}Rh, ^{89}Ru, ^{88}Tc, ^{87,88,89}Mo, and ^{87,88,89}Nb. Typical mass resolving powers of 300 000 and 400 000 FWHM were achieved in Experiments I and II, respectively. In Table I, the results are summarized and compared to the literature values given in the AME2020 [45]. In Fig. 2, the deviation from the literature values is graphically shown. In Fig. 3, the mass spectra of ^{89}Ru (Experiments I and II) and of ^{91}Rh (Experiment II) are shown. ^{89}Ru and ^{88}Tc were measured in both experiments. The data taking lasted 18 hours for Experiment I and only 1 hour for Experiment II. Despite the thinner target used in Experiment II, the measured count rate of ^{89}Ru was about ten detected ions per hour, about a factor 3 higher in Experiment II with respect to Experiment I, representing a major

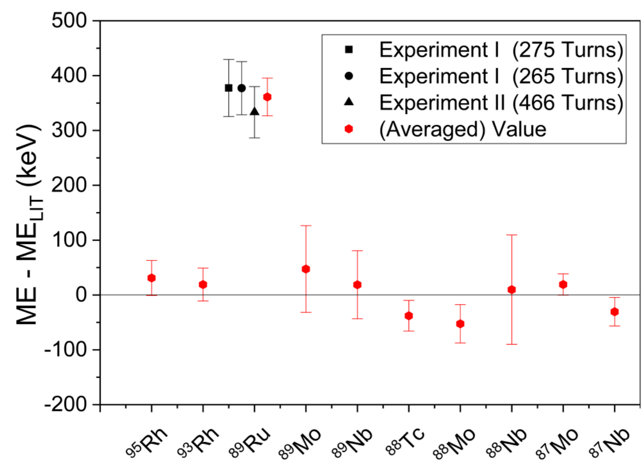

FIG. 2. Measured mass excess deviation from measurements reported in the literature [45] in keV. The values correspond to the last column of Table I. For ^{89}Ru, the individual measurements, two in Experiment I (square and circle symbols) and one in Experiment II (triangle symbol), and their average (hexagon symbol) are included. For the rest of the measured nuclei, all measurements (individual and averaged) agree within their uncertainties and only their average is reported.

improvement, which was the cumulative result of the different primary beam intensities, target thicknesses, FRS operation modes, CSC areal densities, and transmission efficiencies.

A. First mass measurement of ^{91}Rh

This work constitutes the first mass measurement of ^{91}Rh. A total of 44 events for ^{91}Rh were recorded in two measurements with two different turn numbers in Experiment II [Fig. 3(c)]. Odd-even nuclei in this region of the nuclear chart with a ground state with spin-parity of $(9/2^+)$, such as ^{91}Rh, are known to have isomeric states with spin-parity $(1/2^-)$ [48,49]. Based on spectroscopy studies, an isomer with an excitation energy of 172.9(4) keV and a half-life very similar to that of the ground state has been reported for ^{91}Rh [50–53]. This isomer, if populated with a significant fraction, would have been resolved from the ground state in this work, since the FWHM of the observed ^{91}Rh peak is only approximately 200 keV. However, in both measurements, the peak shape does not deviate from the expected single-peak form. The ground states of odd-even nuclei with spin-parity $(9/2^+)$ are known to be populated much more abundantly in fragmentation reactions (>90%) than their isomeric states with spin-parity $(1/2^-)$ [42,49,54–56]. The generally low population of $(1/2^-)$ isomeric states is also confirmed by the mass measurement of ^{93}Rh and ^{95}Rh reported here, both of which have been reported to have $(1/2^-)$ isomeric states with excitation energies of 267(48) keV [49] and 543.3(3) keV [52], respectively. The measurements reported here show no evidence for the presence of an isomeric contribution in ^{93}Rh. For ^{95}Rh, the observed tail structure allows an upper limit of $\lesssim 7\%$, derived using Poisson statistics, to be placed on the isomer-to-ground-state ratio. Therefore, the observed single peaks of rhodium isotopes were all assigned to their ground states. For ^{91}Rh, a mass excess of $-58\,466(20)$ keV was determined.

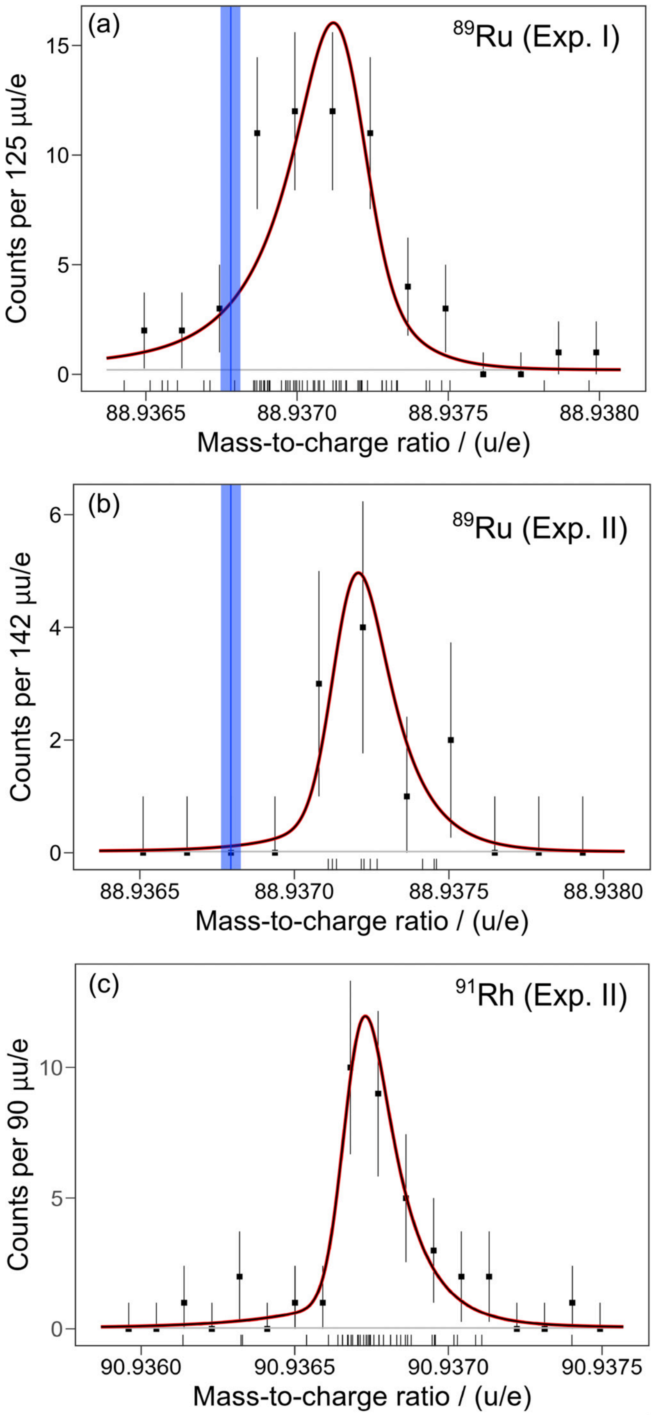

FIG. 3. Measured mass spectra of ^{89}Ru in Experiment I (a), in Experiment II (b) and of ^{91}Rh in Experiment II (c). The square symbols are the binned data used just for representation; the fit was obtained using unbinned data, which are shown as a rug graph at the bottom of each panel. The solid red curve shows the fitted Hyper-EMG probability distribution function, normalized to the number of events in the histogram. In panels (a) and (b), the blue line represents the literature mass value of ^{89}Ru and the blue shadow represents the literature mass uncertainty [45], where the width corresponds to ± one standard deviation.

B. Mass measurement of ^{89}Ru reveals a large deviation from the literature value

The mass value reported in the AME2020 [45] for the ground state of ^{89}Ru is based solely on one direct mass measurement performed with a Penning trap employing the time-of-flight ion cyclotron resonance (TOF-ICR) technique [57]. Penning traps can reach the highest mass resolving powers of all mass spectrometers; however, the mass window covered in Penning trap measurements is usually very narrow. Narrow-band measurements are prone to misidentification, if an unexpected ion species appears in the investigated mass range instead of the expected species; see, e.g., [58–60]. In addition, the TOF-ICR technique has a relatively small dynamic range, which makes it difficult to detect contamination that overlaps with the ion of interest in the scanned resonance and may lead to shifts in the mass measurement. In contrast, MR-TOF-MS can cover a much wider mass-to-charge range [47]. This allows detection and identification of nearby ion species, such as molecular contaminants or isomeric states. It thus gives a better understanding of the different ion species present in the measurement and helps to avoid misidentification.

In this work, the mass of ^{89}Ru was measured two times in Experiment I and once in Experiment II; altogether three different turn numbers were used (Table I), and a total of 71 events were recorded [Fig. 3(a) and 3(b)]. All three individual measurements are found to agree. A weighted average mass excess of −58 008(25) keV was obtained, which yields a deviation of 361(35) keV, corresponding to more than 10 standard deviations, from the previous Penning trap measurement [57]. To exclude misidentification due to potential molecular contamination, the MAVERIC technique developed in this work (see above) was applied to all three measurements. Furthermore, the correct identification of ^{89}Ru is supported by the simultaneous stopping and extraction of the isotones ^{89}Ru and ^{88}Tc in both experiments, which, according to simulations [61], have the same stopping range in the CSC.

For ^{89}Ru, an isomer with spin-parity $(1/2^-)$ and an excitation energy of about 350 keV is predicted based on systematic trends [48,49]; however, so far no experimental evidence for its existence has been reported in the literature. In the measurements in this work, a single peak, narrower than the excitation energy of the predicted isomer, with a width of about 275 and 200 keV FWHM for Experiments I and II, respectively, was measured. This peak was assigned to the ground state with spin-parity $(9/2^+)$ following the same argument above that in this region, ground states of odd-even nuclei with spin-parity $(9/2^+)$ are populated much more abundantly in fragmentation reactions than an isomeric state with spin-parity $(1/2^-)$. This implies that the deviation observed in this work from the literature value cannot be attributed to the assignment of the measured state.

C. Mass measurement of ^{88}Tc, ^{87,88,89}Mo, ^{87,88,89}Nb, and ^{93,95}Rh

For all other mass measurements presented in this work, i.e., ^{88}Tc, ^{87,88,89}Mo, ^{87,88,89}Nb, and ^{93,95}Rh, their individual as well as the given weighted averages agree well with the measurements previously reported in the AME2020 [45]. These measurements, excluding ^{91}Rh and ^{89}Ru, have a weighted average deviation of −5(10) keV and a Birge ratio [62] of 0.84. For the mass and uncertainty determination of ^{88}Nb, ^{89}Nb, and ^{88}Tc, the procedure described in Ref. [45] was followed due to unresolved long-lived isomers with excitation energies of 130(120), 0(30) [52], and 70.4(31) keV [57], respectively. For ^{88}Tc, a single distribution was detected in all three measurements with 532 detected events in total. After the correction for the unresolved isomer following the method in [45], a difference −38(28) keV for the mass of ^{88}Tc to the literature value [45] was calculated. This is an indication that mostly the ground state of ^{88}Tc was populated in this experiment since the method used assumes that both unresolved species are equally populated.

IV. SYSTEMATICS OF THE MASS SURFACE

The measured masses reported in this work were used to study the systematics of the one-proton separation energy (S_p), calculated as shown in Eq. (1), where ME(N, Z) is the mass excess of certain nucleus with N neutrons and Z protons and $\mathrm{ME}_{^1\mathrm{H}}$ is the mass excess of the hydrogen (^{1}H) atom [45]:

$$S_p(N, Z) = \mathrm{ME}(N, Z-1) + \mathrm{ME}_{^1\mathrm{H}} - \mathrm{ME}(N, Z). \quad (1)$$

This observable is studied as a function of Z in the mid-shell region between the proton shell closures at $Z = 28$ and $Z = 50$ for different chains of nuclei with constant half-integer of total isospin projections, $T_z = 1/2$, $3/2$, $5/2$, and $7/2$. The investigation was done for constant isospin projections to allow comparing the S_p values of nuclei that are expected to have similar nuclear structure properties in the studied region of the nuclear chart, including the Island of Inversion around $N = Z = 40$, where the magnitude and rapidity of the shape changes are very sensitive to the similarities of the proton and neutron single-particle energies [6,9,27]. We focus separately on odd- and even-Z nuclei to avoid staggering of the S_p observable; that is, for constant T_z, each S_p point is separated from the next by an α particle ($Z = 2$ and $N = 2$). We include the first mass measurement of ^{91}Rh ($Z = 45, N = 46$) (Sec. IV A) and the new mass value of ^{89}Ru ($Z = 44, N = 45$) (Sec. IV B) measured in this work. For the rest of the nuclei employed in the plots, we include the AME2020 and masses published recently [27,35,63–67].

A. Trends in the one-proton separation energy for odd-Z nuclides

The results of the systematic study of odd-Z nuclei with half-integer isospin projection (i.e., even-N nuclides) are presented in Fig. 4. Here, a steep decrease of the S_p values between $Z = 27$ and $Z = 29$, which is a signature for the closed proton shell at $Z = 28$, is followed by a gradual decrease of this observable for larger Z. In the $T_z = 1/2$ isospin projection chain, this smooth decrease is broken between $Z = 35$ and $Z = 41$ (with a center at around $Z = 38$), and the plot shows a clear change in the trend of the observable. The same effect, although less pronounced, is visible in the $T_z = 3/2$ chain, and for the remaining $T_z = 5/2$ and $7/2$ chains, the

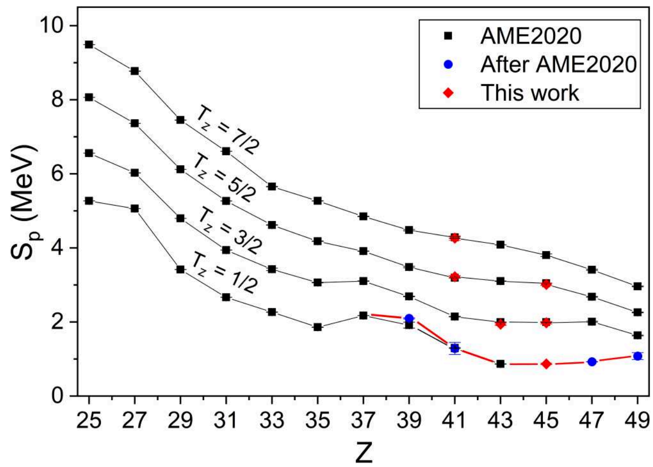

FIG. 4. Calculated one-proton separation energy (S_p) for half-integer total isospin projections (from bottom to top $T_z = 1/2$, $3/2$, $5/2$, and $7/2$) versus odd proton numbers (Z). The data points showing black squares have been calculated using solely nonextrapolated mass excess values reported by the AME2020 [45] and are linked with solid black lines to guide the eye. The red diamonds represent points calculated using at least one mass excess reported in this work. The blue circles represent data points calculated with mass measurements published recently: at $Z = 39$ ^{79}Y and at $Z = 41$ ^{83}Nb from Ref. [63], at $Z = 47$ ^{95}Ag from Ref. [64], and at $Z = 49$ ^{99}In from Ref. [65].

effect vanishes. The rapid shape and nuclear structure changes in the island of inversion around $N = Z = 40$ [4,7–9], including the oblate-prolate shape transition at $N = Z = 36$ [9,10] and the strong prolate deformations in nuclei around $N = Z =$ 38–42 [4,8], might provide an explanation for the observed S_p trends. Above $Z = 43$, the first mass measurement of ^{91}Rh presented in this work, together with masses published after the AME2020 [63–65], complete a smooth trend of the S_p values in the $T_z = 1/2$ isospin projection chain up to $Z = 49$, which is in line with a predicted gradually decreasing deformation towards the doubly magic ^{100}Sn [11,12].

A clear increase of the S_p at $Z \geqslant 45$ for the $T_z = 1/2$ nuclei in Fig. 4, reaching a local maximum at $Z = 49$, can be seen. The increasing trend is also visible for the $T_z = 3/2$, although less pronounced than for the $T_z = 1/2$, where its local maximum is at $Z = 47$. There is no increasing trend but a flattening of the observable for the $T_z = 5/2$ for $Z \geqslant 41$ until a changing point at $Z = 45$ where a clear down slope starts. The flattening of the observable is less pronounced for the $T_z = 7/2$ and ends at a changing point located at $Z = 43$, where again, a decreasing slope (although less pronounced) can be seen. A closed neutron shell $N = 50$ is common to all the nuclei where there is a local maximum or a change from flat to a decreasing slope (for $T_z = 1/2$ at $Z = 49$, for $T_z = 3/2$ at $Z = 47$, for $T_z = 5/2$ at $Z = 45$, and for $T_z = 7/2$ at $Z = 43$). All these fingerprints suggest that the nature of this particular observation lies in the strength of the proton-neutron interaction involving a $N = 50$ nucleus, which is then enhanced when approaching $N = Z$ nuclei due to a larger spatial overlap of their wave functions [27,68].

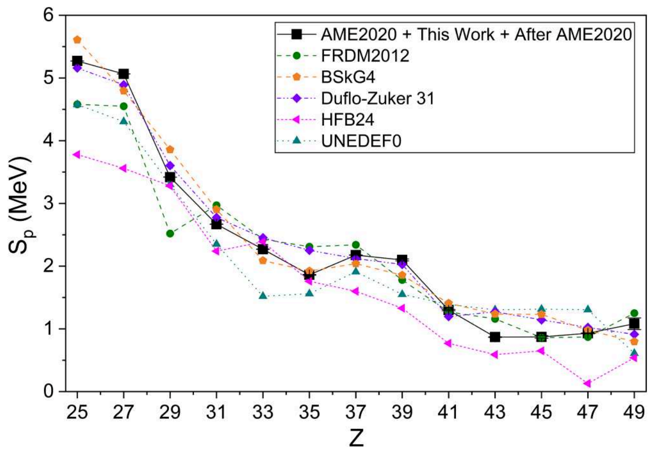

FIG. 5. Comparison of the S_p for $T_z = 1/2$ for odd-Z nuclei calculated including the mass from ^{91}Rh ($Z = 45$) reported in this work and other masses reported after the AME2020 with black symbols and solid lines (^{79}Y and ^{83}Nb from Ref. [63], ^{95}Ag from Ref. [64], and ^{99}In from Ref. [65]) with mass models linked with dotted lines: FRDM2012 [69] with olive green circles, BSkG4 [70] with orange pentagons, DZ31 [71] with violet diamonds, HFB24 [72] with pink left-triangles, and UNEDF0 [73] with dark cyan up-triangles.

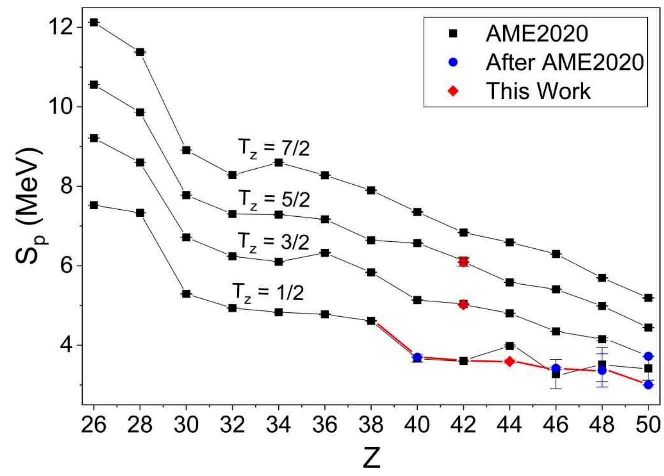

FIG. 6. One-proton separation energy (S_p) for even-Z nuclei calculated for different constant half-integer isospin projection chains, from top to bottom $T_z = 1/2$, $3/2$, $5/2$, and $7/2$. The data points showing black squares are calculated employing solely the nonextrapolated mass excesses reported in the AME2020 [45] and are connected using a black line. The red diamonds are calculated using at least one reported mass excess from this work, as in Table I. The blue circles are calculated employing mass excesses reported recently: for $T_z = 1/2$ at $Z = 40$, ^{81}Zr was taken from Ref. [27]; at $Z = 46$, ^{93}Pd was taken from Ref. [35]; at $Z = 48$, ^{96}Ag was taken from Ref. [64]; at $Z = 50$, ^{100}In was taken from Ref. [65] and ^{101}Sn from Ref. [67]; and for $T_z = 3/2$ at $Z = 50$, the mass of ^{103}Sn was taken from Ref. [66].

The S_p values of the $T_z = 1/2$ chain shown in Fig. 4, including the latest experimental data which shows a clear change of the trend between $Z = 35$ and $Z = 41$ (centered at around $Z = 38$), were compared to calculated values using the mass excesses from different mass models: the latest microscopic-macroscopic finite-range droplet (FRDM2012 [69]), the latest version of the microscopic Brussels-Skyrme-on-a-grid (BSkG4 [70]), the microscopic Duflo-Zuker (DZ) [71], the microscopic Skyrme-Hartree-Fock-Bogoliubov (HFB) [72], and the microscopic UNEDF0 [73]. The comparison is shown in Fig. 5. The general trend is matched by most of the models, and the change of the trend between $Z = 35$ and $Z = 41$ is excellently described (although with less strength) by the BSkG4 mass model.

B. Trends in the one-proton separation energy for even-Z nuclides

The results of the present work for even-Z nuclei with constant half-integer isospin projection (i.e., odd-N nuclides) are shown in Fig. 6.

The step down of the S_p between $Z = 28$ and $Z = 30$, the signature of the closed proton shell at $Z = 28$, is followed by a second step down between $Z = 38$ and $Z = 40$ in the $T_z = 1/2$ series, whereas all the other isospin projection chains show a smooth decrease with increasing atomic number. The observed step in the $T_z = 1/2$ series can be attributed to a deformed subshell gap at $Z = 38$, which occurs at large prolate deformations [5–7,26] and is enhanced by a coherent action of proton and neutron shell effects [6,9,20]. The trend of the S_p values at this deformed subshell gap shows a very similar step effect as at the well-known $Z = 28$ closed proton shell, but with only about half of the magnitude due to its difference in nature. With the previous mass value of ^{89}Ru [57], this fingerprint seen as a unique step between two well-known closed shells, $Z = 28$ and $Z = 50$, would be questionable because of the substantial increase of the S_p value at $Z = 44$. Only due to the new mass measurement of ^{89}Ru, presented in this work, combined with other recent mass measurements [27,35,64–67], the subshell closure and the further gradual decrease becomes clearly visible. Notably, the observed slightly different S_p trends in $T_z = 1/2$ nuclei with odd and even Z (Figs. 4 and 6) could be an additional indication for rapid shape changes between odd-Z and even-Z nuclei in the island of inversion studied here (around $N = Z = 40$) [8,11,13–16].

In Fig. 7, the experimental S_p values of even-Z nuclides with $T_z = 1/2$ are compared with the predictions of the microscopic-macroscopic mass model FRDM2012 [69] and the microscopic models BSkG4 [70], Duflo-Zuker (DZ) [71], Skyrme-Hartree-Fock-Bogoliubov (HFB) [72], and UNEDF0 [73]. The step between $Z = 38$ to $Z = 40$ is well reproduced only by the FRDM2012 and the BSkG4 models. For the FRDM model, this is presumably due to the inclusion of a new "deformed" region at $N \approx 40$ and $Z \approx 40$ already in the first version (FRDM1981) [74]. For the BSkG model, the BSkG4 version presents a clear improvement in describing the trend compared to its first and second versions (BSkG1 [75] and BSkG2 [76], which are not shown in Fig. 7 to enhance readability). Moreover, the smooth trend in the experimental data for $Z \geqslant 40$ is well reproduced by the FRDM2012 model and partially reproduced by the BSkG4 model, where for $Z > 46$ the slope of this observable seems to be overestimated.

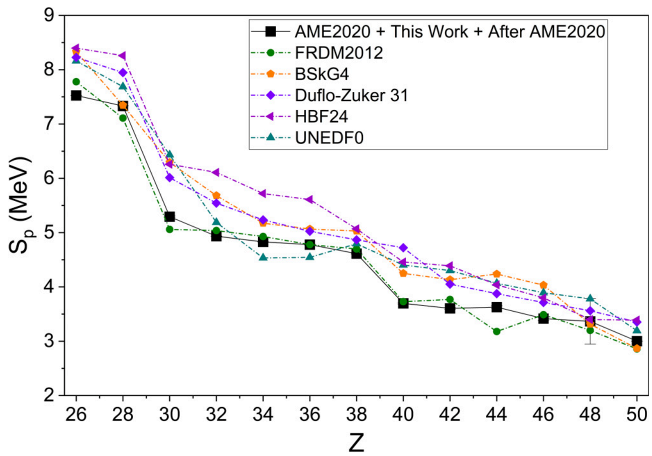

FIG. 7. Comparison of the S_p for $T_z = 1/2$ for even-Z nuclei calculated including the mass from ^{89}Ru ($Z = 44$) reported in this work and other masses reported after the AME2020 with black squares and linked with solid lines (^{81}Zr from Ref. [27], ^{93}Pd from Ref. [35], ^{96}Ag from Ref. [64], ^{100}In from Ref. [65], and ^{101}Sn from Ref. [67]), with mass models linked with dotted lines: FRDM2012 [69] with olive green circles, BSkG4 [70] with orange pentagons, DZ31 [71] with violet diamonds, HFB24 [72] with pink left-triangles and UNEDF0 [73] with dark cyan up-triangles.

V. CONCLUSIONS

The masses of eleven exotic nuclei close to the heavy $N = Z$ region have been measured with the FRS Ion Catcher at GSI. The mass of ^{91}Rh was measured for the first time. For the mass of ^{89}Ru, we have found a discrepancy by more than ten standard deviations with the literature value, where our mass measurement yields a value that is 361(35) keV less bound than that of the previous measurement [45,57]. The masses of the other nuclides presented in this work agree well with previously published data. Misidentification of the measured nuclei, including ^{89}Ru, with a molecular contamination was ruled out using the newly developed MAVERIC method.

To obtain further insights on the rapid changes of the nuclear shapes and related shell effects in the island of inversion around $N = Z = 40$, the measured masses were used to study the systematics of the one-proton separation energy (S_p) in nuclei with constant half-integer total isospin projections (T_z) for odd- and even-Z separately. In the odd-Z, $T_z = 1/2$ nuclei, the mass of ^{91}Rh measured for the first time and reported here, together with other masses measured after the publication of the AME2020, complete the systematics up to the doubly magic ^{100}Sn. A clear change in the trend of S_p values located in the mid-shell region between $Z = 35$ and $Z = 41$ (centered around $Z = 38$) can be seen. In the even-Z, $T_z = 1/2$ nuclei, the new mass of ^{89}Ru presented in this work together with other recent mass measurements smoothens the trend of the S_p values for $Z > 40$ nuclei up to the doubly magic ^{100}Sn. A unique step between $Z = 38$ and $Z = 40$ appears. Both of these observed irregularities in the S_p trends in odd- and even-Z nuclei might point to nuclear shape changes around $Z = 38$, which disperse with increasing T_z values moving away from the $N = Z$ line. For the odd-Z nuclei, the latest version of the microscopic Brussels-Skyrme-on-a-grid model (BSkG4 [70]) excellently reproduces the trend shown by the experimental data, although with less magnitude. For the even-Z nuclei, the microscopic-macroscopic finite-range droplet model FRDM2012 [69] and the BSkG4 model [70] reproduce the S_p trends observed with the latest experimental data.

Further relevance of the ^{89}Ru and ^{91}Rh masses reported in this work, which lies outside the scope of this paper, include the calculation of masses using mass relations of mirror nuclei [77]. Furthermore, an important impact of the mass of ^{91}Rh on the astrophysical rapid-proton capture process in the $A \approx 90$ region is expected [78,79].

ACKNOWLEDGMENTS

The results presented here are based on the experiments S526 and G-22-00056, which were performed at the FRS at the GSI Helmholtzzentrum für Schwerionenforschung, Darmstadt (Germany) in the context of FAIR Phase-0. This work was supported by the German Federal Ministry of Research, Technology and Space (BMFTR) under Contracts No. 05P21RGFN1 and No. 05P24RG4, by the German Research Foundation (DFG) under Contract No. 422761894, by HGS-HIRe, and by Justus-Liebig-Universität Gießen and GSI under the JLU-GSI strategic Helmholtz partnership agreement. The work leading to this publication was supported by the Deutsche Forschungsgemeinschaft (DFG, German Research Foundation, AY 155/2-1) and in part by the ExtreMe Matter Institute EMMI at the GSI Helmholtzzentrum für Schwerionenforschung, Darmstadt, Germany. This project has received funding from the European Union's Horizon Europe Research and Innovation program under Grant Agreements No. 101057511 (EURO-LABS) and No. 771036 (ERC CoG MAIDEN) and from the Research Council of Finland under the Researcher mobility Grants No. 347509, No. 354968, No. 369714, and No. 374065. Z.G. acknowledges support from the Research Council of Finland under Project No. 354589. G.K.-K. and M.P.R. acknowledge the support from the nuclear physics consolidated grant STFC under Grant Agreement No. ST/Y000293/1. The ELI-NP team is supported by the Romanian Ministry of Research, Innovation and Digitalisation under Research Contract PN-23-21-01-06. A.S. and P.C. acknowledge partial financial support by the ELI-RO program, Contracts No. ELI-RO/RDI/2024-007 (ELITE) and No. FAIR-RO/RD/2024_008 (InCellMNT) projects sponsored by the Romanian Ministry of Research, Innovation and Digitalisation. I.C.S. acknowledges partial support by the Romanian Ministry of Research and Innovation, Bucharest, under Grants No. PN-23-21-0102 and No. PNIII-P5-P5.2 of the FAIR-RO program with the NAFRO2 project. J.L.R.-S. acknowledges support from the Xunta de Galicia under the program *Proyectos de excelencia*, Grant No. ED431F-2023/43. I. Mardor acknowledges support for this work from the Israel Science Foundation, Grant No. 2575/21. D. Kar gratefully acknowledges support from the Sandwich Ph.D. program between IIT-ISM Dhanbad, India and GSI GmbH, Darmstadt Germany (Grant No. IIT(ISM)/R&D/Sandwich/PhD/2024/PHYSICS/04), and by the GET_INvolved Programme (Grant No. 2024/11/ISM02). A.A. acknowledges support from the Spanish Ministerio de Ciencia e Innovación under Grant No. PID2022-138297NB-C21 and by the Generalitat Valenciana Prometeo Grant No. CIPROM/2022/9.

DATA AVAILABILITY

The data that support the findings of this article are not publicly available. The data are available from the authors upon reasonable request.

[1] O. Sorlin and M.-G. Porquet, Nuclear magic numbers: New features far from stability, Prog. Part. Nucl. Phys. **61**, 602 (2008).

[2] T. Otsuka, A. Gade, O. Sorlin, T. Suzuki, and Y. Utsuno, Evolution of shell structure in exotic nuclei, Rev. Mod. Phys. **92**, 015002 (2020).

[3] F. Nowacki, A. Poves, E. Caurier, and B. Bounthong, Shape coexistence in ^{78}Ni as the portal to the fifth island of inversion, Phys. Rev. Lett. **117**, 272501 (2016).

[4] J. Ha, F. Recchia, S. M. Lenzi, H. Iwasaki, D. D. Dao, F. Nowacki, A. Revel, P. Aguilera, G. de Angelis, J. Ash, D. Bazin, M. A. Bentley, S. Biswas, S. Carollo, M. L. Cortes, R. Elder, R. Escudeiro, P. Farris, A. Gade, T. Ginter, *et al.*, Abrupt structural transition in exotic molybdenum isotopes unveils an isospin-symmetric island of inversion, Nat. Commun. **16**, 10631 (2025).

[5] W. P. Alford, R. E. Anderson, P. A. Batay-Csorba, D. A. Lind, H. H. Wieman, and C. D. Zafiratos, Structure of ^{88}Sr from the ^{86}Kr(^{3}He, n)^{88}Sr reaction, Nucl. Phys. A **293**, 83 (1977).

[6] J. H. Hamilton, A. V. Ramayya, C. F. Maguire, R. B. Piercey, R. Bengtsson, P. Moller, J. R. Nix, J. ye Zhuang, R. L. Robinson, and S. Frauendorf, Effects of reinforcing shell gaps in the competition between spherical and highly deformed shapes, J. Phys. G: Nucl. Phys. **10**, L87 (1984).

[7] A. Lemasson, H. Iwasaki, C. Morse, D. Bazin, T. Baugher, J. S. Berryman, A. Dewald, C. Fransen, A. Gade, S. McDaniel, A. Nichols, A. Ratkiewicz, S. Stroberg, P. Voss, R. Wadsworth, D. Weisshaar, K. Wimmer, and R. Winkler, Observation of mutually enhanced collectivity in self-conjugate $^{76}_{38}$Sr$_{38}$, Phys. Rev. C **85**, 041303(R) (2012).

[8] R. D. O. Llewellyn, M. A. Bentley, R. Wadsworth, H. Iwasaki, J. Dobaczewski, G. de Angelis, J. Ash, D. Bazin, P. C. Bender, B. Cederwall, B. P. Crider, M. Doncel, R. Elder, B. Elman, A. Gade, M. Grinder, T. Haylett, D. G. Jenkins, I. Y. Lee, B. Longfellow, *et al.*, Establishing the maximum collectivity in highly deformed $N = Z$ nuclei, Phys. Rev. Lett. **124**, 152501 (2020).

[9] J. H. Hamilton, P. G. Hansen, and E. F. Zganjar, Advances in studies of nuclei far from stability, Rep. Prog. Phys. **48**, 631 (1985).

[10] S. M. Fischer, T. Anderson, P. Kerns, G. Mesoloras, D. Svelnys, C. J. Lister, D. P. Balamuth, P. A. Hausladen, and D. G. Sarantites, Shape coexistence in ^{71}Br and the question of the ground-state spin of ^{71}Kr, Phys. Rev. C **72**, 024321 (2005).

[11] K. Kaneko, N. Shimizu, T. Mizusaki, and Y. Sun, Triple enhancement of quasi-SU(3) quadrupole collectivity in strontium-zirconium N ≈ Z isotopes, Phys. Lett. B **817**, 136286 (2021).

[12] M. Górska, Trends in the structure of nuclei near ^{100}Sn, Physics **4**, 364 (2022).

[13] A. J. Nichols, R. Wadsworth, H. Iwasaki, K. Kaneko, A. Lemasson, G. de Angelis, V. M. Bader, T. Baugher, D. Bazin, M. A. Bentley, J. S. Berryman, T. Braunroth, P. J. Davies, A. Dewald, C. Fransen, A. Gade, M. Hackstein, J. Henderson, D. G. Jenkins, D. Miller, *et al.*, Collectivity in A ∼ 70 nuclei studied via lifetime measurements in ^{70}Br and ^{68,70}Se, Phys. Lett. B **733**, 52 (2014).

[14] K. Wimmer, W. Korten, P. Doornenbal, T. Arici, P. Aguilera, A. Algora, T. Ando, H. Baba, B. Blank, A. Boso, S. Chen, A. Corsi, P. Davies, G. de Angelis, G. de France, J.-P. Delaroche, D. T. Doherty, J. Gerl, R. Gernhäuser, M. Girod, *et al.*, Shape changes in the mirror nuclei ^{70}Kr and ^{70}Se, Phys. Rev. Lett. **126**, 072501 (2021).

[15] A. Vitéz-Sveiczer, A. Algora, A. I. Morales, B. Rubio, G. G. Kiss, P. Sarriguren, P. Van Isacker, G. de Angelis, F. Recchia, S. Nishimura, J. Agramunt, V. Guadilla, A. Montaner-Pizá, S. E. A. Orrigo, A. Horváth, D. Napoli, S. Lenzi, A. Boso, V. Phong, J. Wu, *et al.*, The β-decay of ^{70}Kr into ^{70}Br: Restoration of the pseudo-SU(4) symmetry, Phys. Lett. B **830**, 137123 (2022).

[16] S. M. Lenzi, A. Poves, and A. O. Macchiavelli, Shell model analysis of the $B(E2, 2^+ \to 0^+)$ values in the $A = 70$, $T = 1$ triplet ^{70}Kr, ^{70}Br, and ^{70}Se, Phys. Rev. C **104**, L031306 (2021).

[17] P. Van Isacker, D. D. Warner, and D. S. Brenner, Test of Wigner's spin-isospin symmetry from double binding energy differences, Phys. Rev. Lett. **74**, 4607 (1995).

[18] M. Wang, Y. H. Zhang, X. Zhou, X. H. Zhou, H. S. Xu, M. L. Liu, J. G. Li, Y. F. Niu, W. J. Huang, Q. Yuan, S. Zhang, F. R. Xu, Y. A. Litvinov, K. Blaum, Z. Meisel, R. F. Casten, R. B. Cakirli, R. J. Chen, H. Y. Deng, C. Y. Fu, *et al.*, Mass measurement of upper fp-shell $N = Z - 2$ and $N = Z - 1$ nuclei and the importance of three-nucleon force along the $N = Z$ line, Phys. Rev. Lett. **130**, 192501 (2023).

[19] Y. P. Wang, Y. K. Wang, F. F. Xu, P. W. Zhao, and J. Meng, Abnormal bifurcation of the double binding energy differences and proton-neutron pairing: Nuclei close to $N = Z$ line from Ni to Rb, Phys. Rev. Lett. **132**, 232501 (2024).

[20] W. Nazarewicz, J. Dudek, R. Bengtsson, T. Bengtsson, and I. Ragnarsson, Microscopic study of the high-spin behaviour in selected A ≈ 80 nuclei, Nucl. Phys. A **435**, 397 (1985).

[21] A. Petrovici, K. W. Schmid, and A. Faessler, Shape coexistence and shape transition in $N \approx Z$ nuclei from krypton to molybdenum, Nucl. Phys. A **605**, 290 (1996).

[22] P.-G. Reinhard, D. J. Dean, W. Nazarewicz, J. Dobaczewski, J. A. Maruhn, and M. R. Strayer, Shape coexistence and the effective nucleon-nucleon interaction, Phys. Rev. C **60**, 014316 (1999).

[23] L. Gaudefroy, A. Obertelli, S. Péru, N. Pillet, S. Hilaire, J. P. Delaroche, M. Girod, and J. Libert, Collective structure of the $N = 40$ isotones, Phys. Rev. C **80**, 064313 (2009).

[24] T. R. Rodríguez and J. L. Egido, Multiple shape coexistence in the nucleus ^{80}Zr, Phys. Lett. B **705**, 255 (2011).

[25] B. S. Hu, Z. H. Sun, G. Hagen, and T. Papenbrock, *Ab initio* computations of strongly deformed nuclei near ^{80}Zr, Phys. Rev. C **110**, L011302 (2024).

[26] M. Sharma, M. Rajput, S. Singh, A. Bharti, G. H. Bhat, and J. A. Sheikh, Shape evolution of even-even strontium isotopes near $N = 50$ shell closure, Eur. Phys. J. A **61**, 113 (2025).
[27] A. Hamaker, E. Leistenschneider, R. Jain, G. Bollen, S. A. Giuliani, K. Lund, W. Nazarewicz, L. Neufcourt, C. R. Nicoloff, D. Puentes, R. Ringle, C. S. Sumithrarachchi, and I. T. Yandow, Precision mass measurement of lightweight self-conjugate nucleus ^{80}Zr, Nat. Phys. **17**, 1408 (2021).
[28] T. Yamaguchi, H. Koura, Y. Litvinov, and M. Wang, Masses of exotic nuclei, Prog. Part. Nucl. Phys. **120**, 103882 (2021).
[29] R. Kanungo, Shell closures in the N and $Z = 40$–60 region for neutron and proton-rich nuclei, Phys. Lett. B **649**, 31 (2007).
[30] W. R. Plaß, T. Dickel, S. Purushothaman, P. Dendooven, H. Geissel, J. Ebert, E. Haettner, C. Jesch, M. Ranjan, M. P. Reiter, H. Weick, F. Amjad, S. Ayet San Andrés, M. Diwisch, A. Estrade, F. Farinon, F. Greiner, N. Kalantar-Nayestanaki, R. Knöbel, J. Kurcewicz, *et al.*, The FRS Ion Catcher - A facility for high-precision experiments with stopped projectile and fission fragments, Nucl. Instrum. Methods Phys. Res., Sect. B **317**, 457 (2013).
[31] W. R. Plaß, T. Dickel, I. Mardor, S. Pietri, H. Geissel, C. Scheidenberger, D. L. Amanbayev, S. Ayet San Andrés, J. Äystö, D. Balabanski, S. Beck, J. Bergmann, V. Charviakova, P. Constantin, T. Eronen, T. Grahn, F. Greiner, E. Haettner, C. Hornung, J.-P. Hucka, *et al.*, The science case of the FRS Ion Catcher for FAIR Phase-0, Hyperfine Interact. **240**, 73 (2019).
[32] H. Geissel, P. Armbruster, K. Behr, A. Brünle, K. Burkard, M. Chen, H. Folger, B. Franczak, H. Keller, O. Klepper, B. Langenbeck, F. Nickel, E. Pfeng, M. Pfützner, E. Roeckl, K. Rykaczewski, I. Schall, D. Schardt, C. Scheidenberger, K.-H. Schmidt, *et al.*, The GSI projectile fragment separator (FRS): A versatile magnetic system for relativistic heavy ions, Nucl. Instrum. Methods Phys. Res., Sect. B **70**, 286 (1992).
[33] J. Stadlmann, L. Bozyk, P. Forck, D. Ondreka, R. Singh, and P. Spiller, SIS18 operation and recent development, in *Proceedings of IPAC'23*, 14th International Particle Accelerator Conference (JACoW, Geneva, 2023), pp. 1683–1686.
[34] E. Haettner, B. Franczak, H. Geissel, T. Dickel, S. Pietri, W. Plaß, A. Prochazka, S. Purushothaman, C. Scheidenberger, Y. Tanaka, S. Terashima, H. Weick, J. Winfield, and M. Yavor, New high-resolution and high-transmission modes of the FRS for FAIR phase-0 experiments, Nucl. Instrum. Methods Phys. Res., Sect. B **463**, 455 (2020).
[35] G. Kripkó-Koncz, W. R. Plaß, I. Dedes, D. D. Dao, T. Dickel, C. Hornung, D. Amanbayev, S. A. S. Andrés, S. Beck, J. Bergmann, A. Blazhev, J. Dudek, H. Geissel, E. Haettner, N. Kalantar-Nayestanaki, *et al.* (for the Super-FRS Experiment Collaboration), Direct mass measurement of ^{93}Pd and implications for the isomer structures in ^{94}Ag: Tracing the two-proton decay branch, Phys. Rev. Res. **7**, L042022 (2025).
[36] M. Ranjan, S. Purushothaman, T. Dickel, H. Geissel, W. R. Plaß, D. Schäfer, C. Scheidenberger, J. V. de Walle, H. Weick, and P. Dendooven, New stopping cell capabilities: RF carpet performance at high gas density and cryogenic operation, Europhys. Lett. **96**, 52001 (2011).
[37] S. Purushothaman, M. P. Reiter, E. Haettner, P. Dendooven, T. Dickel, H. Geissel, J. Ebert, C. Jesch, W. R. Plaß, M. Ranjan, H. Weick, F. Amjad, S. Ayet San Andrés, M. Diwisch, A. Estrade, F. Farinon, F. Greiner, N. Kalantar-Nayestanaki, R. Knöbel, J. Kurcewicz, *et al.*, First experimental results of a cryogenic stopping cell with short-lived, heavy uranium fragments produced at 1000 MeV/u, Europhys. Lett. **104**, 42001 (2013).
[38] M. Ranjan, P. Dendooven, S. Purushothaman, T. Dickel, M. Reiter, S. Ayet San Andrés, E. Haettner, I. Moore, N. Kalantar-Nayestanaki, H. Geissel, W. Plaß, D. Schäfer, C. Scheidenberger, F. Schreuder, H. Timersma, J. Van de Walle, and H. Weick, Design, construction and cooling system performance of a prototype cryogenic stopping cell for the Super-FRS at FAIR, Nucl. Instrum. Methods Phys. Res., Sect. A **770**, 87 (2015).
[39] W. R. Plaß, T. Dickel, U. Czok, H. Geissel, M. Petrick, K. Reinheimer, C. Scheidenberger, and M. Yavor, Isobar separation by time-of-flight mass spectrometry for low-energy radioactive ion beam facilities, Nucl. Instrum. Methods Phys. Res., Sect. B **266**, 4560 (2008).
[40] W. R. Plaß, T. Dickel, and C. Scheidenberger, Multiple-reflection time-of-flight mass spectrometry, Int. J. Mass Spectrom. **349-350**, 134 (2013).
[41] T. Dickel, W. R. Plaß, A. Becker, U. Czok, H. Geissel, E. Haettner, C. Jesch, W. Kinsel, M. Petrick, C. Scheidenberger, A. Simon, and M. I. Yavor, A high-performance multiple-reflection time-of-flight mass spectrometer and isobar separator for the research with exotic nuclei, Nucl. Instrum. Methods Phys. Res., Sect. A **777**, 172 (2015).
[42] G. Kripkó-Koncz, Investigation of ground and isomeric states of exotic nuclei using advances in multiple-reflection time-of-flight mass spectrometry: Unraveling riddles surrounding the proton-emitting isomer(s) in ^{94}Ag, Ph.D. thesis, Justus-Liebig-Universität Gießen, 2025, https://doi.org/10.22029/jlupub-20182.
[43] W. Xian, M. Rosenbusch, V. H. Phong, M. Wada, P. Schury, D. Hou, A. Takamine, S. Chen, T. Niwase, Y. Hirayama, H. Ishiyama, S. Iimura, Y. Ito, T. M. Kojima, S. Kimura, J. Liu, J. Lee, S. Michimasa, H. Miyatake, J. Y. Moon, *et al.*, Atomic mass measurements of neutron-rich nuclides on the path to ^{78}Ni with a β-TOF-equipped MRTOF device, Front. Phys. **13**, 1644477 (2025).
[44] S. Ayet San Andrés, C. Hornung, J. Ebert, W. R. Plaß, T. Dickel, H. Geissel, C. Scheidenberger, J. Bergmann, F. Greiner, E. Haettner, C. Jesch, W. Lippert, I. Mardor, I. Miskun, Z. Patyk, S. Pietri, A. Pihktelev, S. Purushothaman, M. P. Reiter, A.-K. Rink, *et al.*, High-resolution, accurate multiple-reflection time-of-flight mass spectrometry for short-lived, exotic nuclei of a few events in their ground and low-lying isomeric states, Phys. Rev. C **99**, 064313 (2019).
[45] M. Wang, W. J. Huang, F. G. Kondev, G. Audi, and S. Naimi, The AME 2020 atomic mass evaluation (II). Tables, graphs and references, Chin. Phys. C **45**, 030003 (2021).
[46] S. Purushothaman, S. Ayet San Andrés, J. Bergmann, T. Dickel, J. Ebert, H. Geissel, C. Hornung, W. R. Plaß, C. Rappold, C. Scheidenberger, Y. K. Tanaka, and M. I. Yavor, Hyper-EMG: A new probability distribution function composed of exponentially modified Gaussian distributions to analyze asymmetric peak shapes in high-resolution time-of-flight mass spectrometry, Int. J. Mass Spectrom. **421**, 245 (2017).
[47] A. Spătaru, G. Kripkó-Koncz, T. Dickel, C. Hornung, W. R. Plaß, P. Constantin, D. Amanbayev, S. Ayet San Andrés, D. L. Balabanski, S. Beck, J. Bergmann, H. Geissel, N. Kalantar-Nayestanaki, J. Kehat, I. Mardor, *et al.*, Broadband mass measurements with the FRS Ion Catcher facility at GSI and

theory developments investigating the shape-phase transition near $N = 90$, Phys. Rev. C **111**, 054307 (2025).

[48] B. Cai, C. Yuan, G. Zhang, Y. Zhang, M. Liu, Y. Xing, X. Xu, J. Li, and M. Wang, Isomeric structure in the ^{100}Sn region: Possible competition between β^+ decay and proton emission in the isomeric unbound nucleus ^{97}Sn, Phys. Rev. C **109**, L051302 (2024).

[49] Y. M. Xing, C. X. Yuan, M. Wang, Y. H. Zhang, X. H. Zhou, Y. A. Litvinov, K. Blaum, H. S. Xu, T. Bao, R. J. Chen, C. Y. Fu, B. S. Gao, W. W. Ge, J. J. He, W. J. Huang, T. Liao, J. G. Li, H. F. Li, S. Litvinov, S. Naimi, *et al.*, Isochronous mass measurements of neutron-deficient nuclei from ^{112}Sn projectile fragmentation, Phys. Rev. C **107**, 014304 (2023).

[50] N. Mărginean, C. Rusu, D. Bucurescu, C. Rossi Alvarez, C. A. Ur, D. Bazzacco, S. Lunardi, P. Pavan, G. d. Angelis, M. Axiotis, E. Farnea, A. Gadea, M. Ionescu-Bujor, A. Iordăchescu, W. Krolas, T. Kröll, S. M. Lenzi, T. Martinez, R. Menegazzo, D. R. Napoli, *et al.*, Identification of excited states and shell model description of the $N = Z + 1$ nucleus ^{91}Rh, Phys. Rev. C **72**, 014302 (2005).

[51] J. Park, R. Krücken, D. Lubos, R. Gernhäuser, M. Lewitowicz, S. Nishimura, D. S. Ahn, H. Baba, B. Blank, A. Blazhev, P. Boutachkov, F. Browne, I. Čeliković, G. de France, P. Doornenbal, T. Faestermann, Y. Fang, N. Fukuda, J. Giovinazzo, N. Goel, *et al.*, New and comprehensive β- and βp-decay spectroscopy results in the vicinity of ^{100}Sn, Phys. Rev. C **99**, 034313 (2019).

[52] F. G. Kondev, M. Wang, W. J. Huang, S. Naimi, and G. Audi, The NUBASE2020 evaluation of nuclear physics properties, Chin. Phys. C **45**, 030001 (2021).

[53] S. Garg, B. Maheshwari, B. Singh, Y. Sun, A. Goel, and A. K. Jain, Atlas of nuclear isomers—Second edition, At. Data Nucl. Data Tables **150**, 101546 (2023).

[54] A. Mollaebrahimi, C. Hornung, T. Dickel, D. Amanbayev, G. Kripko-Koncz, W. R. Plaß, S. Ayet San Andrés, S. Beck, A. Blazhev, J. Bergmann, H. Geissel, M. Górska, H. Grawe, F. Greiner, E. Haettner, N. Kalantar-Nayestanaki, I. Miskun, F. Nowacki, C. Scheidenberger, S. Bagchi, *et al.*, Studying Gamow-Teller transitions and the assignment of isomeric and ground states at $N = 50$, Phys. Lett. B **839**, 137833 (2023).

[55] D. Amanbayev, Mass measurements at the N=Z and N=126 limits at the FRS Ion Catcher and development of the cryogenic stopping cell for the Super-FRS, Ph.D. thesis, Justus-Liebig-Universität Gießen, 2023, https://doi.org/10.22029/jlupub-18567.

[56] C. Hornung, D. Amanbayev, I. Dedes, G. Kripko-Koncz, I. Miskun, N. Shimizu, S. Ayet San Andrés, J. Bergmann, T. Dickel, J. Dudek, J. Ebert, H. Geissel, M. Górska, H. Grawe, F. Greiner, E. Haettner, T. Otsuka, W. R. Plaß, S. Purushothaman, A.-K. Rink, *et al.*, Isomer studies in the vicinity of the doubly-magic nucleus ^{100}Sn: Observation of a new low-lying isomeric state in ^{97}Ag, Phys. Lett. B **802**, 135200 (2020).

[57] M. Vilén, A. Kankainen, P. Baczyk, L. Canete, J. Dobaczewski, T. Eronen, S. Geldhof, A. Jokinen, M. Konieczka, J. Kostensalo, I. D. Moore, D. A. Nesterenko, H. Penttilä, I. Pohjalainen, M. Reponen, S. Rinta-Antila, A. de Roubin, W. Satuła, and J. Suhonen, High-precision mass measurements and production of neutron-deficient isotopes using heavy-ion beams at IGISOL, Phys. Rev. C **100**, 054333 (2019).

[58] W. S. Porter, B. Ashrafkhani, J. Bergmann, C. Brown, T. Brunner, J. D. Cardona, D. Curien, I. Dedes, T. Dickel, J. Dudek, E. Dunling, G. Gwinner, Z. Hockenbery, J. D. Holt, C. Hornung, *et al.*, Mapping the $N = 40$ island of inversion: Precision mass measurements of neutron-rich Fe isotopes, Phys. Rev. C **105**, L041301 (2022).

[59] M. Stryjczyk, A. Jaries, A. Kankainen, and T. Eronen, Comment on “Spin-trap isomers in deformed, odd-odd nuclei in the light rare-earth region near $N = 98$”, Phys. Rev. C **111**, 049801 (2025).

[60] S. Kimura, M. Wada, H. Haba, Y. Hirayama, H. Ishiyama, Y. Ito, T. Niwase, M. Rosenbusch, P. Schury, H. Ueno, Y. X. Watanabe, and Y. Yamanouchi, New ground state in ^{149}La removes two-neutron-separation-energy anomaly in lanthanum isotopes, Phys. Rev. Lett. **136**, 232501 (2026).

[61] O. B. Tarasov and D. Bazin, Lise++: Radioactive beam production with in-flight separators, Nucl. Instrum. Methods Phys. Res., Sect. B **266**, 4657 (2008).

[62] R. T. Birge, The calculation of errors by the method of least squares, Phys. Rev. **40**, 207 (1932).

[63] S. Kimura, M. Wada, C. Y. Fu, N. Fukuda, Y. Hirayama, D. S. Hou, S. Iimura, H. Ishiyama, Y. Ito, S. Kubono, K. Kusaka, S. Michimasa, H. Miyatake, S. Nishimura, T. Niwase, V. Phong, M. Rosenbusch, H. Schatz, P. Schury, Y. Shimizu, *et al.*, Precision mass measurements around ^{84}Mo rule out ZrNb cycle formation in the rapid proton-capture process at type I x-ray bursts, Phys. Rev. Lett. **135**, 152701 (2025).

[64] Z. Ge, M. Reponen, T. Eronen, B. Hu, M. Kortelainen, A. Kankainen, I. Moore, D. Nesterenko, C. Yuan, O. Beliuskina, L. Cañete, R. de Groote, C. Delafosse, T. Dickel, A. de Roubin, S. Geldhof, W. Gins, J. D. Holt, M. Hukkanen, A. Jaries, *et al.*, High-precision mass measurements of neutron deficient silver isotopes probe the robustness of the $N = 50$ shell closure, Phys. Rev. Lett. **133**, 132503 (2024).

[65] M. Mougeot, D. Atanasov, J. Karthein, R. N. Wolf, P. Ascher, K. Blaum, K. Chrysalidis, G. Hagen, J. D. Holt, W. J. Huang, G. R. Jansen, I. Kulikov, Y. A. Litvinov, D. Lunney, V. Manea, T. Miyagi, T. Papenbrock, L. Schweikhard, A. Schwenk, T. Steinsberger, *et al.*, Mass measurements of $^{99-101}$In challenge ab initio nuclear theory of the nuclide ^{100}Sn, Nat. Phys. **17**, 1099 (2021).

[66] C. M. Ireland, F. M. Maier, G. Bollen, S. E. Campbell, X. Chen, H. Erington, N. D. Gamage, M. J. Gutiérrez, C. Izzo, E. Leistenschneider, E. M. Lykiardopoulou, R. Orford, W. S. Porter, D. Puentes, M. Redshaw, R. Ringle, S. Rogers, S. Schwarz, L. Stackable, C. S. Sumithrarachchi, *et al.*, High-precision mass measurement of ^{103}Sn restores smoothness of the mass surface, Phys. Rev. C **111**, 014314 (2025).

[67] C. M. Ireland, G. Bollen, S. E. Campbell, X. Chen, H. Erington, N. D. Gamage, K. Godbey, A. M. Houff, C. Izzo, B. Knight, S. Lalit, E. Leistenschneider, E. M. Lykiardopoulou, F. M. Maier, W. Nazarewicz, R. Orford, W. S. Porter, C. Quick, A. Ravlić, M. Redshaw, *et al.*, Mass of ^{101}Sn and Bayesian extrapolations to the proton drip line, Phys. Rev. C **113**, L021302 (2026).

[68] W. Satuła, D. Dean, J. Gary, S. Mizutori, and W. Nazarewicz, On the origin of the Wigner energy, Phys. Lett. B **407**, 103 (1997).

[69] P. Möller, A. J. Sierk, T. Ichikawa, and H. Sagawa, Nuclear ground-state masses and deformations: FRDM (2012), At. Data Nucl. Data Tables **109-110**, 1 (2016).

[70] G. Grams, N. N. Shchechilin, A. Sánchez-Fernández, W. Ryssens, N. Chamel, and S. Goriely, Skyrme–Hartree–Fock–Bogoliubov mass models on a 3D mesh: IV. Improved

description of the isospin dependence of pairing, Eur. Phys. J. A **61**, 35 (2025).
[71] J. Duflo and A. P. Zuker, Microscopic mass formulas, Phys. Rev. C **52**, R23 (1995).
[72] S. Goriely, N. Chamel, and J. M. Pearson, Further explorations of Skyrme-Hartree-Fock-Bogoliubov mass formulas. XII. Stiffness and stability of neutron-star matter, Phys. Rev. C **82**, 035804 (2010).
[73] M. Kortelainen, J. McDonnell, W. Nazarewicz, P.-G. Reinhard, J. Sarich, N. Schunck, M. V. Stoitsov, and S. M. Wild, Nuclear energy density optimization: Large deformations, Phys. Rev. C **85**, 024304 (2012).
[74] P. Möller and J. Rayford Nix, Atomic masses and nuclear ground-state deformations calculated with a new macroscopic-microscopic model, At. Data Nucl. Data Tables **26**, 165 (1981).
[75] G. Scamps, S. Goriely, E. Olsen, M. Bender, and W. Ryssens, Skyrme-Hartree-Fock-Bogoliubov mass models on a 3D mesh: Effect of triaxial shape, Eur. Phys. J. A **57**, 333 (2021).
[76] W. Ryssens, G. Scamps, S. Goriely, and M. Bender, Skyrme–Hartree–Fock–Bogoliubov mass models on a 3D mesh: II. Time-reversal symmetry breaking, Eur. Phys. J. A **58**, 246 (2022).
[77] Y. Y. Zong, C. Ma, M. Q. Lin, and Y. M. Zhao, Mass relations of mirror nuclei for both bound and unbound systems, Phys. Rev. C **105**, 034321 (2022).
[78] A. Parikh, J. José, G. Sala, and C. Iliadis, Nucleosynthesis in type I X-ray bursts, Prog. Part. Nucl. Phys. **69**, 225 (2013).
[79] H. Schatz and W.-J. Ong, Dependence of X-ray burst models on nuclear masses, Astrophys. J. **844**, 139 (2017).